Design Rules for Efficient Metallic Mid Infrared Transparent Electrode Dedicated to Nanocrystal-based Devices

Tung Huu Dang, Mariarosa Cavallo, Adrien Khalili, Erwan Bossavit, Huichen Zhang, Yoann Prado, Claire Abadie, Erwan Dandeu, Sandrine Ithurria, Grégory Vincent, et al.

Design Rules for Efficient Metallic Mid Infrared Transparent Electrode Dedicated to Nanocrystal-based Devices

Tung Huu Dang[1,2], Mariarosa Cavallo[1], Adrien Khalili[1], Erwan Bossavit[1], Huichen Zhang[1], Yoann Prado[1], Claire Abadie[1], Erwan Dandeu[1], Sandrine Ithurria[4], Grégory Vincent[5], Yanko Todorov[2], Carlo Sirtori[2], Angela Vasanelli[2*], Emmanuel Lhuillier[1*]

[1] Sorbonne Université, CNRS, Institut des NanoSciences de Paris, 4 place Jussieu, 75005 Paris, France.
[2] Laboratoire de physique de l'Ecole Normale Supérieure, ENS, Université PSL, CNRS, Sorbonne Université, Université Paris Cité, 24 Rue Lhomond, 75005 Paris, France
[4] Laboratoire de Physique et d'Etude des Matériaux, ESPCI, PSL Research University, Sorbonne Université, CNRS UMR 8213, 10 rue Vauquelin, 75005 Paris, France.
[5] DOTA, ONERA, Université Paris Saclay, 6 Chemin de la Vauve aux Granges, 91120 Palaiseau, France.

Abstract: Colloidal nanocrystals are becoming an increasingly viable alternative to epitaxially grown semiconductors for infrared optoelectronics. Nanocrystal-based imagers have reached a commercial status in the short-wave infrared, while the mid-wave infrared (3-5 µm) appears as a promising playground. Beyond the evident requirement of growing less confined particles, the design of the sensor architecture for colloidal materials requires a complete overhaul compared to their visible and near-infrared counterparts. Here, we focus on designing transparent conductive electrodes in a spectral range where transparent conductive oxides become inefficient. We propose an optimized design of a metallic multi-resonant grating that allows a strong spatial overlap between the confined electromagnetic field and the built-in electrostatic field from a diode stack, thus simultaneously enhancing light absorption and charge collection. The device is then expanded to a 2D metasurface to prevent polarization dependence for maximized light absorption. Finally, we explore the lateral size downscaling of this type of resonator and show its behavior when the size matches the pixel size of infrared focal plane arrays.

Keywords: light-matter coupling, mid-infrared, nanocrystals, photoresponse, pixel.

*To whom correspondence should be sent:angela.vasanelli@ens.fr, el@insp.upmc.fr

INTRODUCTION

While nanocrystals (NCs) have proven to be effective in visible optoelectronics, their potential benefits in the infrared (IR) range are also promising. Concepts developed for the visible range can often be extended to the near-IR with minimal alterations in device architecture, primarily by replacing wide bandgap nanocrystals with narrower bandgap ones. However, the transition to the mid-IR appears more complex. The inherently narrow bandgap characteristics of nanocrystals needed for addressing the mid-IR spectrum demands a complete reassessment of basic device structures, such as diode stacks. For instance, the charge transport layers effective in the visible range can act as tunnel barriers when combined with narrow bandgap materials. Consequently, one of the focal points for achieving efficient diodes in this spectral range has been the in-depth investigation into their band alignment properties[1,2] to develop suitable photodiodes[3–5].

Nevertheless, optimizing band alignment is not the only requirement for efficient mid-infrared nanocrystal-based devices; optical considerations also hold significant importance. In terms of photodetection, photodiodes remain unmatched in their signal-to-noise ratio, necessitating the use of partly transparent electrodes. Transparent conductive oxides (TCOs), widely utilized in the visible and near-IR ranges,[6] employ materials like tin-doped indium oxide (ITO), known for high transparency and low sheet resistance. However, as depicted in Figure S1, the transparency of ITO drops below 40% (resp. below 20%) at 5 µm in wavelength for 50 nm (resp. 100 nm) thick ITO films. This level of transparency prohibits the design of high quantum efficiency devices.

Table 1 Various technology of partly transparent mid infrared electrodes

Technology	Transparency in MWIR	conductivity	Processability	References
Transparent conductive oxide (ITO, FTO)	Weak	High		[6]
CuI/conductive polymer (PEDOT)	Rather focus on visible range	Strongly depend on actual technology	Strongly depend on actual technology	[7–9]
Graphene	High	High	moderate	[10,11]
Array of metallic wires	Mostly for visible and near IR	High	Depend on metal and matrix	[12,13]
Metallic grid	moderate	High	easy	
Resonant metallic grid	High	High	Require e-beam	[14]

Metallic electrodes, as well as graphene, array of metallic wires, cuprous iodide or conductive polymers (see Table 1) can be used as an alternative to TCOs, though most of them have been designed for the visible range and their potential in the mid IR remains mostly unexplored. However, a simplistic design of metallic electrodes often leads to limited transparency due to the metal filling factor. In addition, they introduce a planar component to charge transport, which can be particularly disadvantageous when using nanocrystals featuring short diffusion lengths (typically below 100 nm). An efficient strategy to overcome the filling factor bottleneck is to leverage the concept of extraordinary transmission[15] and optical resonances in metallic or dielectric structures.[16–20] Recent efforts have focused extensively on coupling nanocrystal films to sub-wavelength photonic

structures. The primary goal is to enhance absorption,[21–24] shape spectral responses,[25,26] and even induce bias-tunable photoresponses.[27–29]

In the mid-IR, only a few efforts have been devoted to address the challenge of electrode transparency. A recent study by Dang et al. explored this idea by coupling an HgTe nanocrystal photodiode to a sapphire substrate featuring a metallic grating.[14] The optimized grating geometry generates multiple resonances which significantly increases absorption across a broad spectrum. The resulting absorption surpassed the transparency levels of ITO in the 3-5 µm spectral range, as demonstrated in Figure 1b. However, in this grating design, the low filling factor (metal-to-space ratio) was chosen to favor optical transmission. This choice resulted in a poor overlap between the electromagnetic field and the static electric built-in field, which was detrimental to charge conduction.

Here, we aim to explore how the geometry of the metallic grating can be engineered to achieve both strong absorption and efficient charge conduction. Furthermore, considering the potential transfer of this concept to infrared focal plane arrays, we investigate scaling down the developed grating to sizes compatible with current infrared pixel pitches.

RESULTS AND DISCUSSION

In order to emphasize the criticality of meticulous design for transparent conductive electrodes in mid-IR colloidal detectors, we focus on HgTe NCs,[30–32] recognized as the most advanced colloidal material for addressing the 3-5 µm range, which corresponds to one of the atmospheric transparency windows. Rigorous demonstrations of devices operating in the 3-5 µm range and employing HgTe NCs have elevated the reliability of this material, rendering it usable as an infrared-active spin-coatable ink.[33,34] In our study, the material exhibits an excitonic feature at 3 µm (cut-off at 4 µm, refer to Figure S1). Upon cooling to the conventional operating temperature range for MWIR devices (80-150 K), the cut-off extends to 5 µm. The HgTe NC layer is the MWIR absorbing layer within the diode stack,[35] forming a multilayer structure composed of sapphire/ITO/HgTe/Hg:Ag_2Te/gold (see **Figure 1**a). Here, Hg:Ag_2Te refers to Ag_2Te NCs after Hg cation exchange that act as the hole extraction layer. In a polycrystalline material like a NC film, this configuration optimizes transport across the device's thickness, which is typically a few hundred nanometers.

However, the associated absorption map reveals two main bottlenecks. The chosen thickness, due to transport and fabrication considerations, remains below the material absorption depth[36–38] (several µm). Hence, unless the thickness is carefully chosen to form a Fabry Perot cavity,[23,37,39] the absorption of incident light within the NC layer remains only partial, and losses in the metal can be significant. An alternative approach is to involve resonant gratings (**Figure 1**b and c). Such gratings can generate a designer surface plasmon whose resonance wavelength is determined by the grating's periodicity. In order to generate an effective increase in the photoconductive properties, the resonance wavelength is typically chosen to match the NC band edge. **Figure 1**b presents a grating with a low metal filling factor. In this configuration, the surface plasmon’s electric field changes sign atop the metallic pad, cancelling its magnitude and causing zero absorption atop the pad, where the charge collection path is shortest.

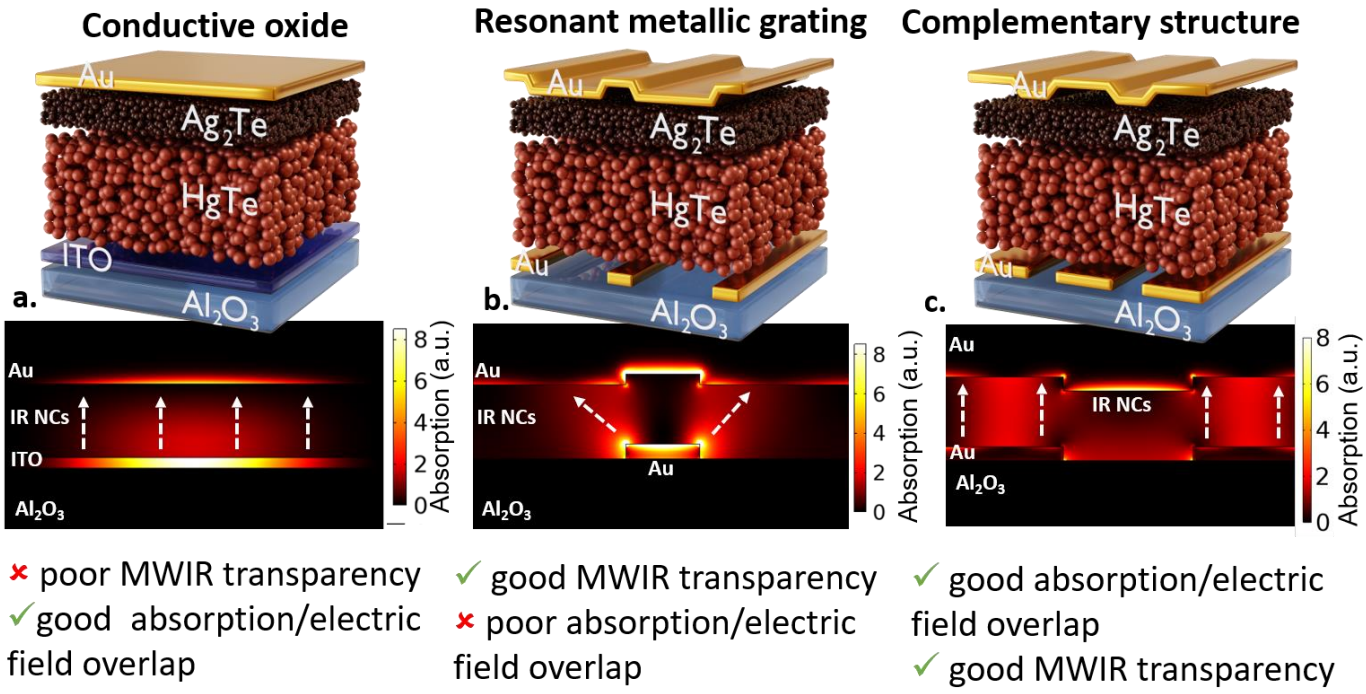

Figure 1 Concept of metallic electrode for mid-IR nanocrystal-based diodes*. Combination of device schematic (top) and associated absorption map (bottom) for device with transparent electrode made of ITO (a.), a low-filling factor resonant grating (b.), and a high-filling factor resonant grating or complementary structure (c.). The white dashed arrows indicate the electrical current directions.*

When employing a low filling factor for the grating, excitons tend to be generated away from the electrode, resulting in a mixture of vertical and planar transport, reducing charge collection efficiency. Hence, designing a grating with a higher filling factor favors charge collection. By carefully choosing the geometrical parameters, a high-filling factor grating can maintain a transmission comparable to a low-filling factor grating. Here, we refer to the high-filling factor grating as a complementary structure (*i.e.*, the large openings in the low-filling factor grating are now replaced with metal stripes, and vice versa). **Figure 1**c shows that a surface plasmon mode in such a high filling factor metallic grating localizes atop the electrode, facilitating a strong overlap between the electromagnetic and the diode's built-in electrostatic fields. Additionally, Figure S4 demonstrates how a higher metal ratio confines the electromagnetic mode more effectively in the NC layer, preventing leakage into the substrate. Moreover, this increase in effective absorption occurs while maintaining nearly constant losses in the metal (Figure S5).

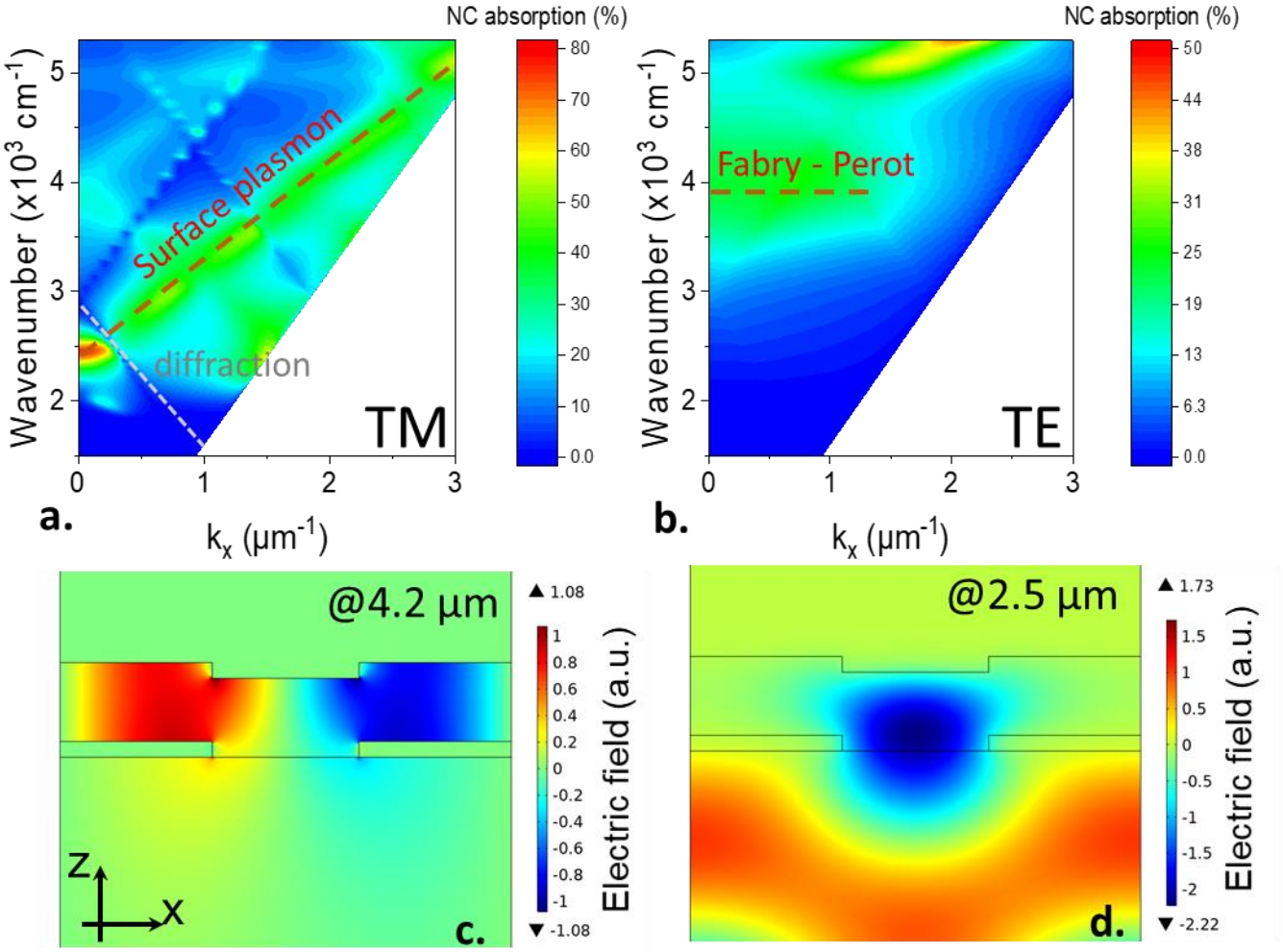

Figure 2 Modal investigation of multi-resonant high-filling-factor 1D grating used to shape mid-IR absorption of the NC-based diode. *a. Dispersion map in TM polarization. b. Dispersion map in TE polarization. c. Electric field component E_z at the maximum of absorption (at 4.2 μm) for TM polarization. d. Electric field component E_y at the maximum of absorption (at 2.5 μm) for TE polarization. The size of the opening is o=0.65 μm, while the period is p=2 μm.*

We investigated the optical characteristics of the mode generated by the high-filling factor grating. Our approach involved simulating the dispersion map and absorption map at the resonance, as shown in **Figure 2**. The TM dispersion map (**Figure 2**a) unveils a dispersive mode whose energy aligns with the NC band edge at normal incidence. This mode corresponds to a surface plasmon, evidenced by the absorption map in **Figure 2**c. Notably, this mode exhibits the highest intensity, with effective absorption (*i.e.*, absorption in the NC film) reaching nearly 80% of the incident light at normal incidence. The weaker absorption at large incidence angles is due to diffraction: incident light gets diffracted above the diffraction limit, resulting in a weaker overall NC absorption. This is shown more clearly in dispersion maps of structures with different grating periods (see Figure S6).

On the other hand, the TE polarization reveals a resonance occurring at a higher energy (4000 cm^{-1} or 2.5 μm or 0.5 eV, as shown in **Figure 2**b) that appears to exhibit a non-dispersive behavior, typically observed for Fabry-Perot resonances. The associated absorption map (**Figure 2**d) indicates that this mode primarily exists between the bottom gold electrodes, in the opening region, due to the optical index discontinuity.

Considering the disparity in effective absorption magnitude between the two resonances, expanding the concept of complementary structure in two dimensions holds significant promise as it could offer a polarization-independent response. Furthermore, a structure that generates surface plasmons in different directions will enable a strong band edge absorption enhancement. Nevertheless, this process is not straightforward. Directly transforming the 1D high-filling factor grating into a 2D grid of large square patches preserves the good optical transmission of the complementary structure while maintaining the high filling factor of the electrode. However, this leads to discontinuity of the metal layer, which is not favorable for electrical connections, see Figure S8. On the other hand, a 2D surface with small square openings does not facilitate a good optical transmission, as shown in Figure S9. This aligns with the conventional understanding that a high-filling factor grid gives rise to high reflection due to excessive metal coverage. In order to achieve higher transmission with a high-filling factor 2D structure, we interconnected the large patches using small wires, as depicted in the right part of **Figure 3**a. This arrangement resulted in the formation of an array of cross openings, as shown in **Figure 3**b-c. Detailed fabrication steps can be found in Figure S10. Similar to the 1D grating with a high filling factor, the electric field primarily localizes over the top of the metal with the 2D metasurface, see **Figure 3**d, ensuring a strong overlap between the electromagnetic field and the built-in static electric field.

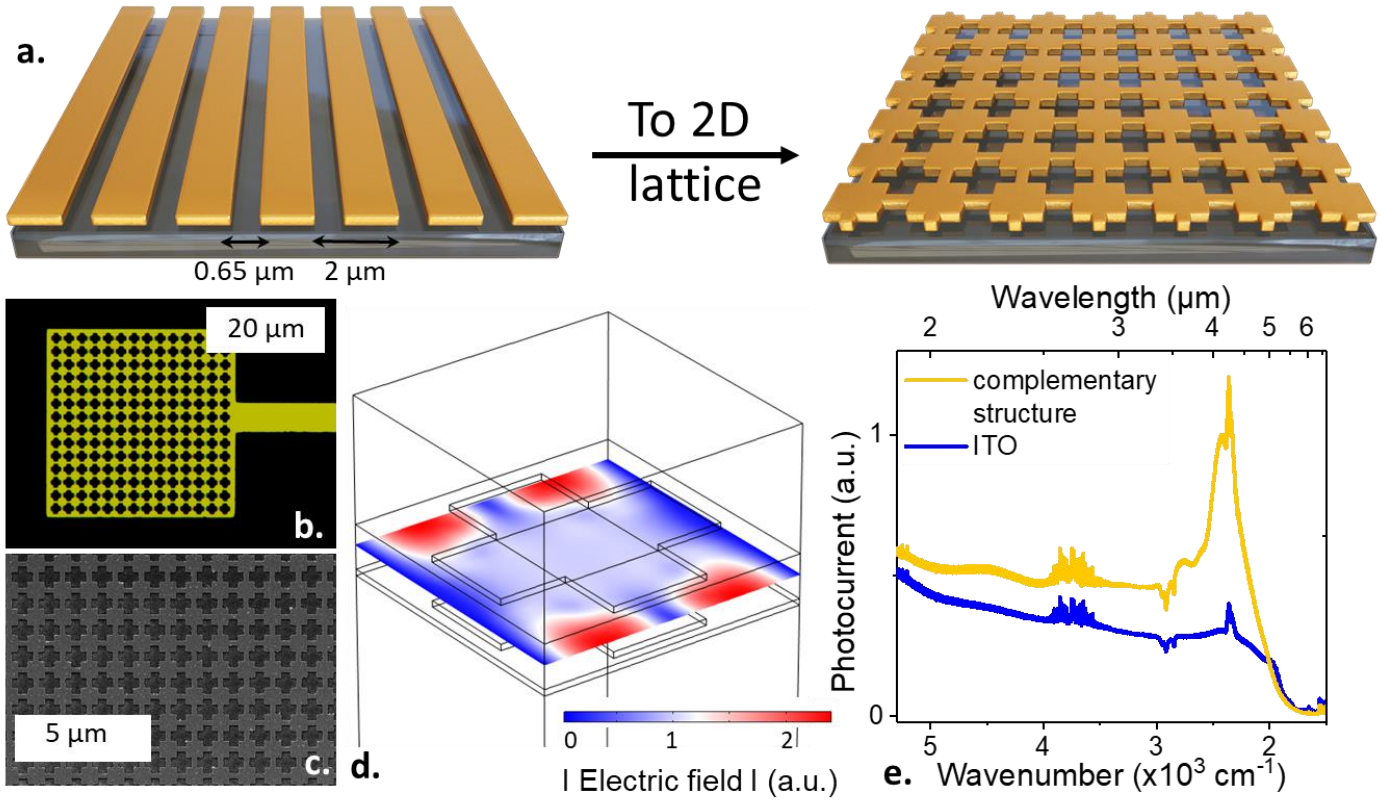

Figure 3 High-filling factor 2D metasurface. *a. Schematic of the 1D high-filling factor grating and the 2D metasurface. b. (resp c.) Optical (resp. Scanning electron microscopy) image of the high-filling factor 2D metasurface. d. Electric field across the NC film, simulated for 2D metasurface bottom electrode with high metal filling factor. e. Photocurrent spectra for the diode with 2D metasurface bottom electrode and a reference device with ITO electrode, measured at 80K, with same gain.*

The overall benefit of the 2D metasurface is better highlighted by comparing the spectral response of the same diode stack using 2D metasurface with that using ITO electrode, as shown in **Figure 3**e. The 2D structure exhibits a strong resonance that spectrally aligns with the NC band edge. Furthermore, the advantage of the resonant metallic grid is not limited to the band edge; the diode's

response improves across the probed spectral range (1.8 µm to 5 µm) compared to the ITO-based diode thanks to the improved transmission. Figure S11 and S12 present complete performance characterization of the diode. At 100 K, the responsivity reaches 2 $A.W^{-1}$, with a detectivity of $3x10^{11}$ Jones and a response time below 100 ns. These photodetection performances are on par with the best NC-based devices operating in the mid-IR.[14,40,41]

Beyond demonstrating a strategy to replace poorly transparent conductive oxides in the mid-IR, another objective of this work is to identify resonator strategies that can later be transferred to the focal plane array (FPA) level. Recently, HgTe NCs have been identified as a viable platform for infrared imagers.[42–46] Transferring the NC film from single-pixel geometry to the surface of a readout integrated circuit (ROIC) poses significant constraints on the lateral size of the device. ROIC pitches typically range around 15 µm for VGA format[42–46] (640x512 pixels) and can be even smaller, down to 10 µm for megapixel imagers[46]. To date, this spatial constraint has limited the types of light-trapping strategies implemented onto the FPA primarily to vertical Fabry-Perot resonance. In the latter case, absorption enhancement is achieved by matching the optical path length with a multiple of λ/2. While the concept is reasonably straightforward on a flat substrate, it becomes more complex on the ROIC due to the roughness brought by electrodes, in addition to the multilayer nature of a diode structure. Therefore, our goal is to develop alternative resonator types that are compatible with lateral size downscaling.

In the following, we explore how the resonance of the 2D complementary metasurface is affected by a size reduction. While the quasi-infinite grid displays a narrow peak aligned with the band edge, we observe broadening and a decrease in magnitude as the lateral size is reduced. However, even for the smallest size with 2x2 periods (*i.e.*, area of 5 µm x 5 µm), the response in the mid-wave infrared (3-5 µm range) still presents a clear resonant feature, in contrast to the device with the ITO electrode, see **Figure 4**a. This indicates the effect of surface plasmon resonance, which can be generated even in a metallic structure with only a few periods.[14] **Figure 4**b shows that absorption enhancement can still be obtained in such a small-sized device. Similar to the quasi-infinite structure (**Figure 3**d), the field enhancement mainly occurs on top of the metal (**Figure 4**c), preserving the overlap between light absorption and charge conduction. This excellent overlap enables a major part of the photocurrent signal to originate from the area with an enhanced field, particularly beneficial in the case of low-mobility materials such as HgTe NC film. We thus achieved an improved signal-to-noise ratio for photodetection with a device whose size is readily comparable with FPA pixel pitch, clearly evidenced by the resonant peak in the photocurrent spectrum.

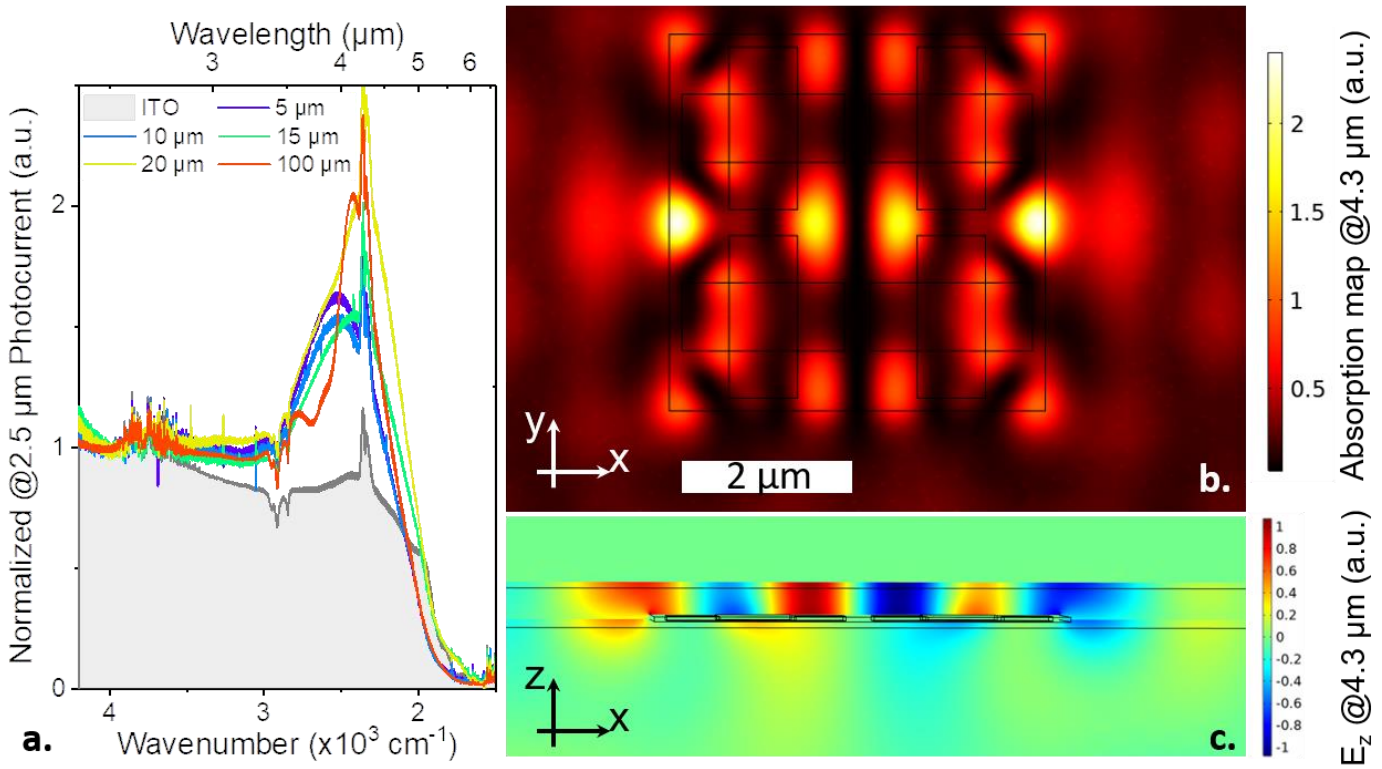

Figure 4 Down scaling resonator to size compatible with pixel pitch*. a. Photocurrent spectra for various lateral extension (from 5 to 100 µm) of the high-filling factor 2D metasurface. For sake of comparison, the spectra obtained with ITO (i.e., without resonance at band edge) is also shown. b. (resp c.) In plane (resp. vertical) absorption map (resp. electric field map) for a 2D structure with lateral extension of 5 µm (i.e. contains only 4 crosses).*

Conclusion

We have designed a strategy for a metallic grating as a partially mid-IR transparent and conductive electrode. It challenges the simplistic notion that transparency is solely driven by the metal filling factor. Instead, this work demonstrates that the high-filling factor in the grating plays a crucial role in enhancing the spatial overlap between light absorption and the static built-in electric field. By coupling two distinct resonance types (Fabry-Perot and surface plasmon), this approach enables a broadband enhancement of NC absorption. Extending this concept to a 2D metasurface demonstrates a threefold increase in resonance-enhanced absorption at the band edge compared to the conventionally used ITO electrode. Furthermore, showcasing the scalability of such resonators to sizes compatible with pixel geometry is a promising prospect. This advancement paves the way for the integration of nanophotonic concepts into focal plane arrays, enabling not only enhanced absorption across the array but also individual spectral filtering on each pixel.

DATA AVAILABILITY

The data that support the findings of this study are available from the corresponding author upon request.

ACKNOWLEDEGMENTS

The project is supported by ERC grant blackQD (grant n° 756225) and AQDtive (grant n°101086358). We acknowledge the use of clean-room facilities from the “Centrale de Proximité Paris-Centre” and support from Renatech for micro and nanofabrication. This work was supported by French state funds managed by the ANR through the grants Frontal (ANR-19-CE09-0017), Graskop (ANR-19-CE09-0026), Copin (ANR-19-CE24-0022), Bright (ANR-21-CE24-0012-02), MixDferro (ANR-21-CE09-0029), Operatwist (ANR-22-CE09-0037-01) and E-map (ANR-23-CE50). This project has received financial support from the CNRS through the MITI interdisciplinary programs (project WITHIN).

COMPETING INTEREST

The authors declare no competing interests.

Supporting Information

Supporting Information include (*i*) methods, (ii) characterization of ITO and HgTe NCs in the mid infrared, (i*ii*) electromagnetic design of gratings (*iv*) discussion on strategies to switch from 1D grating to 2D grid, (*v*) description of diode fabrication and (*vi*) optoelectronic characterization of diode.

REFERENCES

(1) Chen, M.; Guyot-Sionnest, P. Reversible Electrochemistry of Mercury Chalcogenide Colloidal Quantum Dot Films. *ACS Nano* **2017**, *11* (4), 4165–4173. https://doi.org/10.1021/acsnano.7b01014.

(2) Jagtap, A.; Martinez, B.; Goubet, N.; Chu, A.; Livache, C.; Gréboval, C.; Ramade, J.; Amelot, D.; Trousset, P.; Triboulin, A.; Ithurria, S.; Silly, M. G.; Dubertret, B.; Lhuillier, E. Design of a Unipolar Barrier for a Nanocrystal-Based Short-Wave Infrared Photodiode. *ACS Photonics* **2018**, *5* (11), 4569–4576. https://doi.org/10.1021/acsphotonics.8b01032.

(3) Yang, J.; Lv, Y.; He, Z.; Wang, B.; Chen, S.; Xiao, F.; Hu, H.; Yu, M.; Liu, H.; Lan, X.; Hsu, H.-Y.; Song, H.; Tang, J. Bi_2S_3 Electron Transport Layer Incorporation for High-Performance Heterostructure HgTe Colloidal Quantum Dot Infrared Photodetectors. *ACS Photonics* **2023,** 10 (7), 2226–2233. https://doi.org/10.1021/acsphotonics.2c01145.

(4) Rastogi, P.; Izquierdo, E.; Gréboval, C.; Cavallo, M.; Chu, A.; Dang, T. H.; Khalili, A.; Abadie, C.; Alchaar, R.; Pierini, S.; Cruguel, H.; Witkowski, N.; Utterback, J. K.; Brule, T.; Xu, X. Z.; Hollander, P.; Ouerghi, A.; Gallas, B.; Silly, M. G.; Lhuillier, E. Extended Short-Wave Photodiode Based on CdSe/HgTe/Ag_2Te Stack with High Internal Efficiency. *J. Phys. Chem. C* **2022**, *126* (32), 13720–13728. https://doi.org/10.1021/acs.jpcc.2c02044.

(5) Gréboval, C.; Izquierdo, E.; Abadie, C.; Khalili, A.; Cavallo, M.; Chu, A.; Dang, T. H.; Zhang, H.; Lafosse, X.; Rosticher, M.; Xu, X. Z.; Descamps-Mandine, A.; Ouerghi, A.; Silly, M. G.; Ithurria, S.; Lhuillier, E. HgTe Nanocrystal-Based Photodiode for Extended Short-Wave Infrared Sensing with Optimized Electron Extraction and Injection. *ACS Appl. Nano Mater.* **2022**, *5* (6), 8602–8611. https://doi.org/10.1021/acsanm.2c02103.

(6) Maniyara, R. A.; Graham, C.; Paulillo, B.; Bi, Y.; Chen, Y.; Herranz, G.; Baker, D. E.; Mazumder, P.; Konstantatos, G.; Pruneri, V. Highly Transparent and Conductive ITO Substrates for near Infrared Applications. *APL Mater.* **2021**, *9* (2), 021121. https://doi.org/10.1063/5.0040864.

(7) Grundmann, M.; Schein, F.-L.; Lorenz, M.; Böntgen, T.; Lenzner, J.; von Wenckstern, H. Cuprous Iodide – a *p*-Type Transparent Semiconductor: History and Novel Applications. *Phys. Status Solidi A* **2013**, *210* (9), 1671–1703. https://doi.org/10.1002/pssa.201329349.

(8) Liu, A.; Zhu, H.; Kim, M.-G.; Kim, J.; Noh, Y.-Y. Engineering Copper Iodide (CuI) for Multifunctional p-Type Transparent Semiconductors and Conductors. *Adv. Sci.* **2021**, *8* (14), 2100546. https://doi.org/10.1002/advs.202100546.

(9) Lee, J. H.; Jeong, Y. R.; Lee, G.; Jin, S. W.; Lee, Y. H.; Hong, S. Y.; Park, H.; Kim, J. W.; Lee, S.-S.; Ha, J. S. Highly Conductive, Stretchable, and Transparent PEDOT:PSS Electrodes Fabricated with Triblock Copolymer Additives and Acid Treatment. *ACS Appl. Mater. Interfaces* **2018**, *10* (33), 28027–28035. https://doi.org/10.1021/acsami.8b07287.
(10) Gréboval, C.; Noumbé, U. N.; Chu, A.; Prado, Y.; Khalili, A.; Dabard, C.; Dang, T. H.; Colis, S.; Chaste, J.; Ouerghi, A.; Dayen, J.-F.; Lhuillier, E. Gate Tunable Vertical Geometry Phototransistor Based on Infrared HgTe Nanocrystals. *Appl. Phys. Lett.* **2020**, *117* (25), 251104. https://doi.org/10.1063/5.0032622.
(11) Li, X.; Sun, T.; Zhou, K.; Hong, X.; Tang, X.; Wei, D.; Feng, W.; Shen, J.; Wei, D. Broadband InSb/Si Heterojunction Photodetector with Graphene Transparent Electrode. *Nanotechnology* **2020**, *31* (31), 315204. https://doi.org/10.1088/1361-6528/ab884c.
(12) Oh, M.; Jin, W.-Y.; Jun Jeong, H.; Jeong, M. S.; Kang, J.-W.; Kim, H. Silver Nanowire Transparent Conductive Electrodes for High-Efficiency III-Nitride Light-Emitting Diodes. *Sci. Rep.* **2015**, *5* (1), 13483. https://doi.org/10.1038/srep13483.
(13) Bellet, D.; Lagrange, M.; Sannicolo, T.; Aghazadehchors, S.; Nguyen, V. H.; Langley, D. P.; Muñoz-Rojas, D.; Jiménez, C.; Bréchet, Y.; Nguyen, N. D. Transparent Electrodes Based on Silver Nanowire Networks: From Physical Considerations towards Device Integration. *Materials* **2017**, *10* (6), 570. https://doi.org/10.3390/ma10060570.
(14) Dang, T. H.; Cavallo, M.; Khalili, A.; Dabard, C.; Bossavit, E.; Zhang, H.; Ledos, N.; Prado, Y.; Lafosse, X.; Abadie, C.; Gacemi, D.; Ithurria, S.; Vincent, G.; Todorov, Y.; Sirtori, C.; Vasanelli, A.; Lhuillier, E. Multiresonant Grating to Replace Transparent Conductive Oxide Electrode for Bias Selected Filtering of Infrared Photoresponse. *Nano Lett.* **2023**, *23* (18), 8539–8546. https://doi.org/10.1021/acs.nanolett.3c02306.
(15) Lezec, H. J.; Degiron, A.; Devaux, E.; Linke, R. A.; Martin-Moreno, L.; Garcia-Vidal, F. J.; Ebbesen, T. W. Beaming Light from a Subwavelength Aperture. *Science* **2002**, *297* (5582), 820–822. https://doi.org/10.1126/science.1071895.
(16) Lien, M. R.; Wang, N.; Wu, J.; Soibel, A.; Gunapala, S. D.; Wang, H.; Povinelli, M. L. Resonant Grating-Enhanced Black Phosphorus Mid-Wave Infrared Photodetector. *Nano Lett.* **2022**, *22* (21), 8704–8710. https://doi.org/10.1021/acs.nanolett.2c03469.
(17) Gureghian, C.; Vincent, G.; Rodriguez, J.-B.; Sombrio, G.; Gonzalez-Posada, F.; Ribet-Mohamed, I.; Taliercio, T. Dark Current Reduction with All-Semiconductors Nanostructured Type-II Superlattice LWIR Photodetector; SPIE, 2023; Vol. 12430, pp 173–179.
(18) Goldflam, M. D.; Ruiz, I.; Howell, S. W.; Tauke-Pedretti, A.; Anderson, E. M.; Wendt, J. R.; Finnegan, P.; Hawkins, S.; Coon, W.; Fortune, T. R.; Shaner, E. A.; Kadlec, C.; Olesberg, J. T.; Klem, J.; Webster, P. T.; Sinclair, M. B.; Kim, J. K.; Peters, D. W.; Beechem, T. E. Monolithically Fabricated Tunable Long-Wave Infrared Detectors Based on Dynamic Graphene Metasurfaces. *Appl. Phys. Lett.* **2020**, *116* (19), 191102. https://doi.org/10.1063/5.0007780.
(19) Petluru, P.; Muhowski, A. J.; Kamboj, A.; Mansfield, N. C.; Bergthold, M.; Shaner, E. A.; Klem, J. F.; Wasserman, D. All-Epitaxial Resonant Cavity Enhanced Long-Wave Infrared Detectors for Focal Plane Arrays. *Appl. Phys. Lett.* **2023**, *122* (2), 021101. https://doi.org/10.1063/5.0131628.
(20) Palaferri, D.; Todorov, Y.; Bigioli, A.; Mottaghizadeh, A.; Gacemi, D.; Calabrese, A.; Vasanelli, A.; Li, L.; Davies, A. G.; Linfield, E. H. Room-Temperature 9-µm-Wavelength Photodetectors and GHz-Frequency Heterodyne Receivers. *Nature* **2018**, *556* (7699), 85–88.
(21) Abadie, C.; Paggi, L.; Fabas, A.; Khalili, A.; Dang, T. H.; Dabard, C.; Cavallo, M.; Alchaar, R.; Zhang, H.; Prado, Y.; Bardou, N.; Dupuis, C.; Xu, X. Z.; Ithurria, S.; Pierucci, D.; Utterback, J. K.; Fix, B.; Vincent, G.; Bouchon, P.; Lhuillier, E. Helmholtz Resonator Applied to Nanocrystal-Based Infrared Sensing. *Nano Lett.* **2022**, *22* (21), 8779–8785. https://doi.org/10.1021/acs.nanolett.2c02769.
(22) Yifat, Y.; Ackerman, M.; Guyot-Sionnest, P. Mid-IR Colloidal Quantum Dot Detectors Enhanced by Optical Nano-Antennas. *Appl. Phys. Lett.* **2017**, *110* (4), 041106. https://doi.org/10.1063/1.4975058.

(23) Tang, X.; Ackerman, M. M.; Shen, G.; Guyot-Sionnest, P. Towards Infrared Electronic Eyes: Flexible Colloidal Quantum Dot Photovoltaic Detectors Enhanced by Resonant Cavity. *Small* **2019**, *15* (12), 1804920. https://doi.org/10.1002/smll.201804920.
(24) Chen, M.; Shao, L.; Kershaw, S. V.; Yu, H.; Wang, J.; Rogach, A. L.; Zhao, N. Photocurrent Enhancement of HgTe Quantum Dot Photodiodes by Plasmonic Gold Nanorod Structures. *ACS Nano* **2014**, *8* (8), 8208–8216. https://doi.org/10.1021/nn502510u.
(25) Dang, T. H.; Abadie, C.; Khalili, A.; Gréboval, C.; Zhang, H.; Prado, Y.; Xu, X. Z.; Gacemi, D.; Descamps-Mandine, A.; Ithurria, S.; Todorov, Y.; Sirtori, C.; Vasanelli, A.; Lhuillier, E. Broadband Enhancement of Mid-Wave Infrared Absorption in a Multi-Resonant Nanocrystal-Based Device. *Adv. Opt. Mater.* **2022**, *10* (9), 2200297. https://doi.org/10.1002/adom.202200297.
(26) Tang, X.; Ackerman, M. M.; Guyot-Sionnest, P. Acquisition of Hyperspectral Data with Colloidal Quantum Dots. *Laser Photonics Rev.* **2019**, *13* (11), 1900165. https://doi.org/10.1002/lpor.201900165.
(27) Dang, T. H.; Vasanelli, A.; Todorov, Y.; Sirtori, C.; Prado, Y.; Chu, A.; Gréboval, C.; Khalili, A.; Cruguel, H.; Delerue, C.; Vincent, G.; Lhuillier, E. Bias Tunable Spectral Response of Nanocrystal Array in a Plasmonic Cavity. *Nano Lett.* **2021**, *21* (15), 6671–6677. https://doi.org/10.1021/acs.nanolett.1c02193.
(28) Dang, T. H.; Khalili, A.; Abadie, C.; Gréboval, C.; Cavallo, M.; Zhang, H.; Bossavit, E.; Utterback, J. K.; Dandeu, E.; Prado, Y.; Vincent, G.; Ithurria, S.; Todorov, Y.; Sirtori, C.; Vasanelli, A.; Lhuillier, E. Nanocrystal-Based Active Photonics Device through Spatial Design of Light-Matter Coupling. *ACS Photonics* **2022**, *9* (7), 2528–2535. https://doi.org/10.1021/acsphotonics.2c00738.
(29) Dang, T. H.; Abadie, C.; Chu, A.; Cavallo, M.; Khalili, A.; Dabard, C.; Bossavit, E.; Zhang, H.; Prado, Y.; Pierucci, D.; Utterback, J. K.; Todorov, Y.; Sirtori, C.; Jaeck, J.; Vincent, G.; Vasanelli, A.; Fix, B.; Lhuillier, E. Bias Reconfigurable Photoresponse of an Infrared Nanocrystal Film Integrated into a Coupled Fabry-Perot Resonator. *ACS Photonics* **2023**, *10* (5), 1601–1607. https://doi.org/10.1021/acsphotonics.3c00214.
(30) Gréboval, C.; Chu, A.; Goubet, N.; Livache, C.; Ithurria, S.; Lhuillier, E. Mercury Chalcogenide Quantum Dots: Material Perspective for Device Integration. *Chem. Rev.* **2021**, *121* (7), 3627–3700. https://doi.org/10.1021/acs.chemrev.0c01120.
(31) Tian, Y.; Luo, H.; Chen, M.; Li, C.; Kershaw, S. V.; Zhang, R.; Rogach, A. L. Mercury Chalcogenide Colloidal Quantum Dots for Infrared Photodetection: From Synthesis to Device Applications. *Nanoscale* **2023**, *15* (14), 6476–6504. https://doi.org/10.1039/D2NR07309A.
(32) Hao, Q.; Ma, H.; Xing, X.; Tang, X.; Wei, Z.; Zhao, X.; Chen, M. Mercury Chalcogenide Colloidal Quantum Dots for Infrared Photodetectors. *Materials* **2023**, *16* (23), 7321. https://doi.org/10.3390/ma16237321.
(33) Martinez, B.; Ramade, J.; Livache, C.; Goubet, N.; Chu, A.; Gréboval, C.; Qu, J.; Watkins, W. L.; Becerra, L.; Dandeu, E.; Fave, J. L.; Méthivier, C.; Lacaze, E.; Lhuillier, E. HgTe Nanocrystal Inks for Extended Short-Wave Infrared Detection. *Adv. Opt. Mater.* **2019**, *7* (15), 1900348. https://doi.org/10.1002/adom.201900348.
(34) Chen, M.; Lan, X.; Tang, X.; Wang, Y.; Hudson, M. H.; Talapin, D. V.; Guyot-Sionnest, P. High Carrier Mobility in HgTe Quantum Dot Solids Improves Mid-IR Photodetectors. *ACS Photonics* **2019**, *6* (9), 2358–2365. https://doi.org/10.1021/acsphotonics.9b01050.
(35) Ackerman, M. M.; Tang, X.; Guyot-Sionnest, P. Fast and Sensitive Colloidal Quantum Dot Mid-Wave Infrared Photodetectors. *ACS Nano* **2018**, *12* (7), 7264–7271. https://doi.org/10.1021/acsnano.8b03425.
(36) Chehaibou, B.; Abadie, C.; Prado, Y.; Xu, X. Z.; Vincent, G.; Gallas, B.; Mugny, G.; Arnaud, A.; Lhuillier, E.; Delerue, C. Modeling HgTe Complex Optical Index from Bulk to Nanocrystal Layers. *J. Phys. Chem. C* **2023**, *127* (28), 13789–13799. https://doi.org/10.1021/acs.jpcc.3c01837.
(37) Rastogi, P.; Chu, A.; Dang, T. H.; Prado, Y.; Gréboval, C.; Qu, J.; Dabard, C.; Khalili, A.; Dandeu, E.; Fix, B.; Xu, X. Z.; Ithurria, S.; Vincent, G.; Gallas, B.; Lhuillier, E. Complex Optical

Index of HgTe Nanocrystal Infrared Thin Films and Its Use for Short Wave Infrared Photodiode Design. *Adv. Opt. Mater.* **2021**, *9*, 2002066.
(38) Lhuillier, E.; Keuleyan, S.; Guyot-Sionnest, P. Optical Properties of HgTe Colloidal Quantum Dots. *Nanotechnology* **2012**, *23* (17), 175705. https://doi.org/10.1088/0957-4484/23/17/175705.
(39) Tang, X.; Ackerman, M. M.; Guyot-Sionnest, P. Thermal Imaging with Plasmon Resonance Enhanced HgTe Colloidal Quantum Dot Photovoltaic Devices. *ACS Nano* **2018**, *12* (7), 7362–7370. https://doi.org/10.1021/acsnano.8b03871.
(40) Peterson, J. C.; Guyot-Sionnest, P. Room-Temperature 15% Efficient Mid-Infrared HgTe Colloidal Quantum Dot Photodiodes. *ACS Appl. Mater. Interfaces* **2023**, *15* (15), 19163–19169. https://doi.org/10.1021/acsami.3c00487.
(41) Chen, M.; Xue, X.; Qin, T.; Wen, C.; Hao, Q.; Tang, X. Universal Homojunction Design for Colloidal Quantum Dot Infrared Photodetectors. *Adv. Mater. Technol.* **2023**, *8* (16), 2300315. https://doi.org/10.1002/admt.202300315.
(42) Alchaar, R.; Khalili, A.; Ledos, N.; Dang, T. H.; Lebreton, M.; Cavallo, M.; Bossavit, E.; Zhang, H.; Prado, Y.; Lafosse, X.; Parahyba, V.; Potet, P.; Darson, D.; Lhuillier, E. Focal Plane Array Based on HgTe Nanocrystals with Photovoltaic Operation in the Short-Wave Infrared. *Appl. Phys. Lett.* **2023**, *123* (5), 051108. https://doi.org/10.1063/5.0157348.
(43) Gréboval, C.; Darson, D.; Parahyba, V.; Alchaar, R.; Abadie, C.; Noguier, V.; Ferré, S.; Izquierdo, E.; Khalili, A.; Prado, Y.; Potet, P.; Lhuillier, E. Photoconductive Focal Plane Array Based on HgTe Quantum Dots for Fast and Cost-Effective Short-Wave Infrared Imaging. *Nanoscale* **2022**, *14* (26), 9359–9368. https://doi.org/10.1039/D2NR01313D.
(44) Buurma, C.; Pimpinella, R. E.; Ciani, A. J.; Feldman, J. S.; Grein, C. H.; Guyot-Sionnest, P. MWIR Imaging with Low Cost Colloidal Quantum Dot Films; SPIE, 2016; Vol. 9933, p 993303.
(45) Zhang, S.; Bi, C.; Qin, T.; Liu, Y.; Cao, J.; Song, J.; Huo, Y.; Chen, M.; Hao, Q.; Tang, X. Wafer-Scale Fabrication of CMOS-Compatible Trapping-Mode Infrared Imagers with Colloidal Quantum Dots. *ACS Photonics* **2023**, *10* (3), 673–682. https://doi.org/10.1021/acsphotonics.2c01699.
(46) Luo, Y.; Tan, Y.; Bi, C.; Zhang, S.; Xue, X.; Chen, M.; Hao, Q.; Liu, Y.; Tang, X. Megapixel Large-Format Colloidal Quantum-Dot Infrared Imagers with Resonant-Cavity Enhanced Photoresponse. *APL Photonics* **2023**, *8* (5), 056109. https://doi.org/10.1063/5.0145374.

For Table of Contents Use Only

Title: Design Rules for Efficient Metallic Mid Infrared Transparent Electrode Dedicated to Nanocrystal-based Devices

Authors: Tung Huu Dang, Mariarosa Cavallo, Adrien Khalili, Erwan Bossavit, Huichen Zhang, Yoann Prado, Claire Abadie, Erwan Dandeu, Sandrine Ithurria, Grégory Vincent, Yanko Todorov, Carlo Sirtori, Angela Vasanelli, Emmanuel Lhuillier

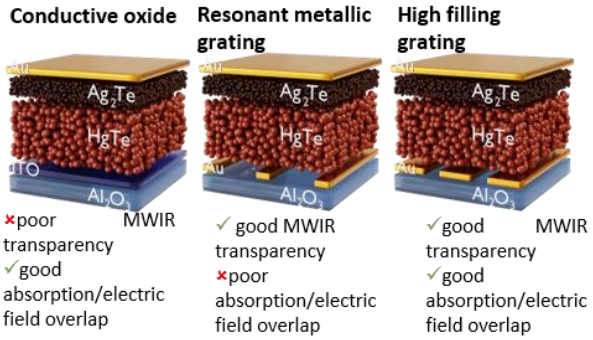

Current work describes how to replace transparent conductive oxide by a metallic grid as partly transparent electrode for mid wave infrared sensing based on nanocrystals while also maintaining optimal built-in electric field beneficial for charge extraction

Supporting information for

Design Rules for efficient Metallic Mid Infrared Transparent Electrode Dedicated to Nanocrystal-based Devices

Tung Huu Dang[1,2], Mariarosa Cavallo[1], Adrien Khalili[1], Erwan Bossavit[1], Huichen Zhang[1], Yoann Prado[1], Claire Abadie[1], Erwan Dandeu[1], Sandrine Ithurria[4], Grégory Vincent[5], Yanko Todorov[2], Carlo Sirtori[2], Angela Vasanelli[2*], Emmanuel Lhuillier[1*]

[1] Sorbonne Université, CNRS, Institut des NanoSciences de Paris, 4 place Jussieu, 75005 Paris, France.
[2] Laboratoire de physique de l'Ecole Normale Supérieure, ENS, Université PSL, CNRS, Sorbonne Université, Université Paris Cité, 24 Rue Lhomond, 75005 Paris, France
[4] Laboratoire de Physique et d'Etude des Matériaux, ESPCI, PSL Research University, Sorbonne Université, CNRS UMR 8213, 10 rue Vauquelin, 75005 Paris, France.
[5] DOTA, ONERA, Université Paris Saclay, 6 Chemin de la Vauve aux Granges, 91120 Palaiseau, France.

*To whom correspondence should be sent: angela.vasanelli@ens.fr, el@insp.upmc.fr

Table of content

1. Method

Chemicals: Mercury chloride ($HgCl_2$, Sigma-Aldrich, 99%), mercury bromide ($HgBr_2$, Alfa Aesar), tellurium powder (Te, Sigma-Aldrich, 99.99%), trioctylphosphine (TOP, Alfa, 90%), oleylamine (OLA, Acros, 80-90%), dodecanethiol (DDT, Sigma-Aldrich, 98%), 2-mercaptoethanol (MPOH, Merck, >99%), and N,N dimethylformamide (DMF, VWR), toluene (VWR, 99.8%) were used. All chemicals were used without further purification, except oleylamine that is centrifuged before use. **Mercury compounds are highly toxic. Handle them with special care.**

1 M TOP:Te precursor: Te powder (6.35 g) was mixed in 50 mL of TOP in a 100 mL three-neck flask. The flask was kept under vacuum at room temperature for 5 mins, then the temperature was raised to 100 °C. Next, degassing of the flask was conducted for the next 20 mins. The atmosphere was switched to nitrogen, and the temperature was raised to 275 °C. The solution was stirred until a clear orange color was obtained. The flask was cooled to room temperature, and the color changed to yellow. Finally, this solution was transferred to a nitrogen-filled glove box for storage.

HgTe NCs growth: In a 100mL three-neck flask, 543 mg of $HgCl_2$ and 50 mL of oleylamine were degassed under vacuum at 110°C. Meanwhile, 2 mL of TOPTe (1M) was extracted from the glove box and mixed with 8 mL of oleylamine. After the flask atmosphere was switched to N_2 and the temperature stabilized at 110°C, the TOPTe solution was quickly injected. After 3 mins, 10 mL of a mixture of DDT in toluene (10% of DDT) was injected, and a water bath was used to quickly decrease the temperature. The content of the flask was split over 3 centrifuge tubes, and MeOH was added. After centrifugation, the formed pellet was redispersed in one centrifuge tube with chloroform. The solution was precipitated a second time using ethanol. The formed pellet was redispersed in chlorobenzene. At this step, the nanocrystals were centrifuged in pure toluene to get rid of the lamellar phase. The solid phase was discarded. The solution is filtered with a 0.2 µm filter.

HgTe ink preparation: 30 mg of $HgCl_2$, 2 mL of MPOH, and 18 mL of DMF are mixed to form an exchange solution. 0.25 mL of this exchange solution and 0.25 mL of DMF are added to 0.25 mL of HgTe NCs in chlorobenzene. Phase dissociation occurs when a few drops of hexane are added to the mixture: the dark bottom phase is where the NCs migrate, while the top transparent phase can be removed with a plastic pipette. This washing step is repeated twice before adding a few mL of toluene, and the mixture is centrifuged at 6000 rpm for 4 minutes. The supernatant is discarded while the formed solid pellets of NCs can be re-dispersed in 100 µL of DMF to obtain the ink of HgTe. A few cycles of sonication – vortex – centrifugation can help to promote particle dispersion. The ink is filtered with a 0.2 µm filter before deposition.

Ag_2Te CQD synthesis: In a 50 mL three-neck flask, 170 mg of $AgNO_3$ are mixed with 25 mL of oleylamine and 2.5 mL of oleic acid. The flask is then degassed under vacuum at room temperature for 15 min and then at 70 °C for 10 mins. The atmosphere is replaced with nitrogen, and 2.5 mL of TOP is added to the solution. Then, the temperature of the flask is raised to 160 °C. After 30 mins, the solution becomes orange. At this step, 0.5 mL of TOP:Te (1M) is injected, and the reaction is quenched

after 10 mins with a water bath. The crude solution is stored in a freezer at -20 °C. When needed, 800 µL of the unfrozen crude solution is precipitated with MeOH. After centrifugation, the formed pellet is redispersed in a mixture containing 200 µL DDT and 600 µL chlorobenzene. Then, the NCs are precipitated by addition of methanol. After centrifugation, the pellet is dispersed using 800 µL of chlorobenzene. Again, the NCs are precipitated by addition of MeOH and centrifugation. The pellet is this time dispersed in 1.6 mL of a (9:1 volume ratio) mixture of hexane:octane.

Infrared Absorption spectroscopy: Absorbance spectra of NC solutions and NC inks are taken with a Fisher IS50 Fourier transform infrared (FTIR) spectrometer. In the attenuated total reflection (ATR) mode, a small amount of NC solution (or NC ink) is dropped on the diamond cell and let to dry. The absorbance spectra are acquired over the range from 7500 cm^{-1} to 500 cm^{-1} with a resolution of 4 cm^{-1}, after averaging over 32 scans.

Transmission electron microscope (TEM) imaging: A drop of diluted NC solution was cast on a copper grid covered with an amorphous carbon film. The grid was degassed overnight under secondary vacuum. A JEOL 2010F system was operated at 200 kV to acquire images.

Reflectivity measurements: The sample is placed under a Brucker Hyperion microscope coupled to a FTIR spectrometer Bruker Vertex 70. The spectrometer is in a reflection configuration under ambient atmosphere and at room temperature. The illumination is provided by a focused Globar source and shines on the device through a Cassegrain objective with incident angles spanning from 12° to 24°. A KBr beam-splitter is used. The detector is a mono-element MCT with a cut-off wavelength of 16 µm that needs to be cooled with liquid nitrogen. The background is acquired on the gold electrodes of the same samples, accounting for the back-side gold mirror. The spectrum is averaged over 64 scans with an 8 cm^{-1} spectral resolution.

Patterning the ITO electrode: Sapphire substrate is rinsed in acetone and isopropanol before being exposed to oxygen plasma for 5 minutes. An ITO layer with a thickness of 50 nm is sputtered on the sapphire substrate. Afterward, the substrate is coated with AZ5214E photoresist at 4000 rpm for 30 seconds, then baked at 110 °C for 90 seconds before UV exposure of 10 seconds for patterning. The resist is developed in AZ726 developer for 30 seconds, forming a mask of 100 µm x 100 µm on top of the ITO layer. The substrate is then dipped in HCl at 40 °C for 35 seconds to etch away the uncovered ITO. The remaining resist is removed by acetone, leaving the ITO area on sapphire.

Macroscopic electrical contacts: Sapphire substrate is rinsed in acetone and isopropanol before exposing to oxygen plasma. A TI prime adhesion layer is spin-coated on the substrate at 4000 rpm for 30 seconds then baked at 120 °C for 2 minutes. AZ5214E photoresist is spin-coated on the substrate at 4000 rpm for 30 seconds, followed by a baking step at 110 °C for 90 seconds. Then, UV exposure with mask is conducted for patterning the photoresist, followed by a step of reversal bake at 126 °C

for 2 minutes and a flood exposure of 40 seconds. The resist is then developed using AZ726 and the substrate is rinsed with DI water. The electrodes are deposited by thermal evaporation of 5 nm Cr and 50 nm Au. The macroscopic Au electrode is connected to the ITO area after this step.

Fabrication of gold grating and grid: 300 nm PMMA is spin-coated and baked at 150 °C for 15 minutes. To prevent the charging effect, a layer of 10 nm Al is evaporated on top of the PMMA layer. A Raith eLine e-beam lithography system is employed for the exposure. The operating voltage is set at 20 kV, and the aperture is set at 10 μm. The dose is set to 180 μC/cm^2. Before resist development, the Al layer is etched with a solution of KOH 10%, and the substrate is rinsed with DI water. The PMMA resist is then developed in a solution of MIBK:IPA (1:3 in volume). The sample is cleaned again with oxygen plasma for 3 minutes before the deposition of 5 nm Cr and 50 nm Au by thermal evaporation. The sample is dipped in an acetone bath overnight, and lift-off is conducted to obtain the metallic grating/grid.

HgTe NC film deposition: A clean substrate with similar size of patterned substrates is used as test substrate for thickness optimization. Before depositing HgTe ink, DMF is spin-coated at 3000 rpm for 30 seconds to increase the adhesion of the HgTe NCs with the substrate surface. The substrate size is typically 15 x 15 mm^2. HgTe film thickness can be adjusted by tuning the rotation speed. The HgTe film is dried under vacuum for at least 2 hours before Ag_2Te deposition.

Ag_2Te NC film deposition: Ag_2Te deposition is conducted as follows: 60 μL of Ag_2Te is gently cast on the HgTe film, followed by a spin-coating step at 1500 rpm for 30 seconds. A few drops of $HgCl_2$ 10 mM are added, and we wait for 15 seconds for the cation exchange process before another spin-coating at 1500 rpm for 30 seconds. The film is then dipped in IPA for 10 seconds and spin-coated at 1500 rpm for 30 seconds for drying. This Ag_2Te/ $HgCl_2$/ IPA treatment is repeated another time, resulting in a 50 nm increase in thickness compared to the initial HgTe film. The deposition is finalized by dipping the film in EDT/ACN (1% in volume) for 30 seconds, followed by the last cleaning step of ACN dipping for 30 seconds. The NCs on top of the macroscopic electrodes are then cleaned with cotton swabs to ensure good electrical contacts for measurements.

Top electrode deposition: A shadow mask is designed for this step such that the top gold layer overlaps with the area of the ITO and Au grating and grid patterns. A gold layer with a thickness of 100 nm is deposited on the area by thermal evaporation.

Electromagnetic simulation: Optical properties of the structure are simulated with COMSOL Multiphysics, 2D Frequency Domain *Interface*. Floquet periodicity is set for boundary conditions at the side edges. A periodic port to generate the incoming electromagnetic wave is placed on the sapphire side. Perfectly matched layers are added to absorb outgoing waves and minimize possible nonphysical reflections due to limited mesh size. Physics-controlled mesh is enabled with extremely fine element size. The dissipated power per unit volume in the metals and nanocrystals can be calculated using the formula $P = 0.5\omega|F|^2\epsilon_0 Im(\varepsilon)$, where F is the electric field, ω

is the angular frequency of the incident wave, ϵ_0 the vacuum permittivity and $Im(\varepsilon)$ the imaginary part of material relative permittivity. The absorption of one material is calculated by integrating the dissipated power over the volume of the material, then divided by the incident power defined in the port. For example, the absorption spectrum in the nanocrystal film is:

$$Abs_{NC}(\omega) = \frac{P_{NC}(\omega)}{P_{incidence}} = \frac{\iiint 0.5\omega|F|^2\epsilon_0 Im(\varepsilon)dV_{NC}}{P_{incidence}}$$

For the sapphire substrate, the real and imaginary parts of the refractive indices are set to 1.73 and 0, respectively. For the gold layer and grating, we used the dielectric function from Drude model ε(E) = 1 – 2.29 x 10^7/ [E(E+i130)], with E the photon energy in meV. This expression of the dielectric permittivity considers the losses due to the NC-metal interface and the presence of the Cr adhesion layer. For the NC film, the real part of the refractive index is set to 2.35 according to ref [37].

Device characterization

Spectral photoresponse is measured with a Fisher IS50 FTIR while the sample is biased with a Femto DLPCA 200 amplifier (0 V bias is applied in case of vertical diodes), which is also used for amplifying the photocurrent signal before sending the signal back into the FTIR for spectral analysis. The spectra are typically obtained in continuous scan mode with 4 cm^{-1} resolution and averaged at least 32 times.

Responsivity is measured with a blackbody at 600 °C as the infrared source. The sample is placed around 40 cm from the blackbody and the incoming flux is modulated by an optical chopper with frequency set to 1000 Hz. A Ge window filtering out all wavelengths shorter than 1.9 μm is placed between the source and the sample. The incident power is then calculated as

$$P(W) = \pi A_{det}.\sin^2\theta/2\,.\cos\varphi.\int_{1.9\mu m}^{\lambda_{cut-off}} \frac{2hc^2}{\lambda^5}\frac{1}{\exp\left(\frac{hc}{\lambda kT}\right)-1}d\lambda$$

where A_{det} is the area of the photodetector, θ is the field of view, φ is the incident angle (typically assumed to be 0º), h is the Planck constant, c is the speed of light, k is Boltzmann constant, T is the blackbody temperature equal to 600 °C. $\lambda_{cut-off}$ is taken from the absorption edge of the material.

Photo response time measurement: The photocurrent signal from the sample (inside the cryostat, placed under voltage bias) is amplified with a DHPCA-100 amplifier then fed to an oscilloscope. The pulses are generated by a MIRsense quantum cascade laser, with a repetition rate of 100 kHz and pulse width of 200 ns.

Noise measurement is conducted with a SR780 spectrum analyzer, while a device is biased with a Femto DLPCA 200 amplifier. The noise spectra are typically acquired

over a frequency range from 10 Hz to 800 Hz. The noise current density spectrum is obtained after averaging 100 scans.

Detectivity is computed from $D^* = \frac{\mathcal{R}\sqrt{A}}{S_I}$, where $\mathcal{R}$ is the responsivity of the device, *A* is the device area (*i.e.*, typically 10^{-4} cm^2 for the quasi-infinite and ITO devices), and S_I is the measured noise current density.

2. Infrared photoactive HgTe nanocrystals and ITO transparency in the spectral region of interest

A typical absorbing material for a mid-wave infrared diode is large HgTe NCs, see **Figure S 1**b. Their band edge at room temperature is around 3 µm (**Figure S 1**a), which redshifts to reach 5 µm cut-off wavelength upon cooling. In the visible and near IR spectral ranges, glass is often a substrate of choice because of its high transparency, low cost, and negligible roughness. However, glass absorption appears problematic beyond 2.5 µm, whereas sapphire substrate[1] presents very good transparency (up to 6 µm) at a reasonable cost. In terms of electrode transparency, using ITO appears problematic in this spectral range, as illustrated in **Figure S 1**a. 50 nm of ITO absorbs about 50 % of the incoming light at 5 µm, asking for alternative electrode materials.

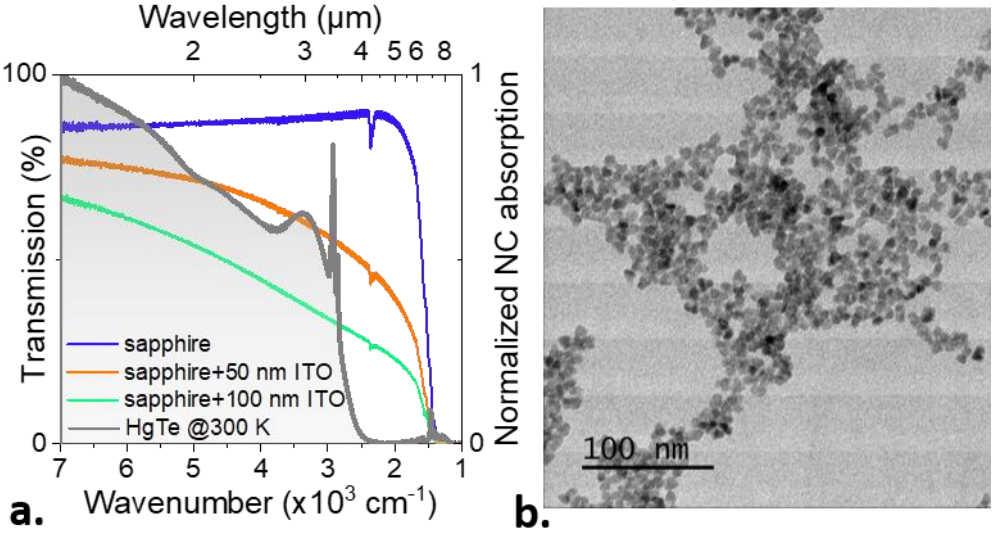

***Figure S 1: IR properties of HgTe NCs and ITO**. a. Absorption spectra of HgTe NCs at room temperature (upon cooling, the spectrum redshifts[2,3]) and transmission of pristine sapphire substrate as well as ITO-coated (thicknesses of 50 nm and 100 nm) sapphire substrate. b. Transmission electron microscopy image of mid-IR HgTe NCs.*

3. Design and comparison between low and high-filling factor gratings

The bottom grating electrode can be defined by grating stripe width *s* and grating period *p,* see **Figure S 2**a. The opening, as a result, can be obtained from *o=p-s*. In the low-filling factor grating used in the mid-IR HgTe-based diode presented in ref. [4], *p* is chosen to be around 1.8 µm - 2 µm to generate a surface plasmon resonance at around 4.5 µm. Thus, *s* is typically less than 0.6 µm to ensure a good transmission of the bottom electrode.[4]

In order to increase the metal filling factor of this electrode, we design a complementary structure in which the large openings in the conventional 1D grating are filled with metal, and the grating stripes are replaced with openings that have the same size, see **Figure S 2**b. Our simulation predicts that, for the complementary structure, surface plasmon at the absorption band edge of the nanocrystals (*i.e.*, around 4.5 µm) can be generated with the period *p* of the grating being around 2 µm, see **Figure S 3**a. This is confirmed by the photocurrent spectra of diodes based on the complementary structure, which are in very good agreement with the simulated NC absorption, as shown in **Figure S 3**b.

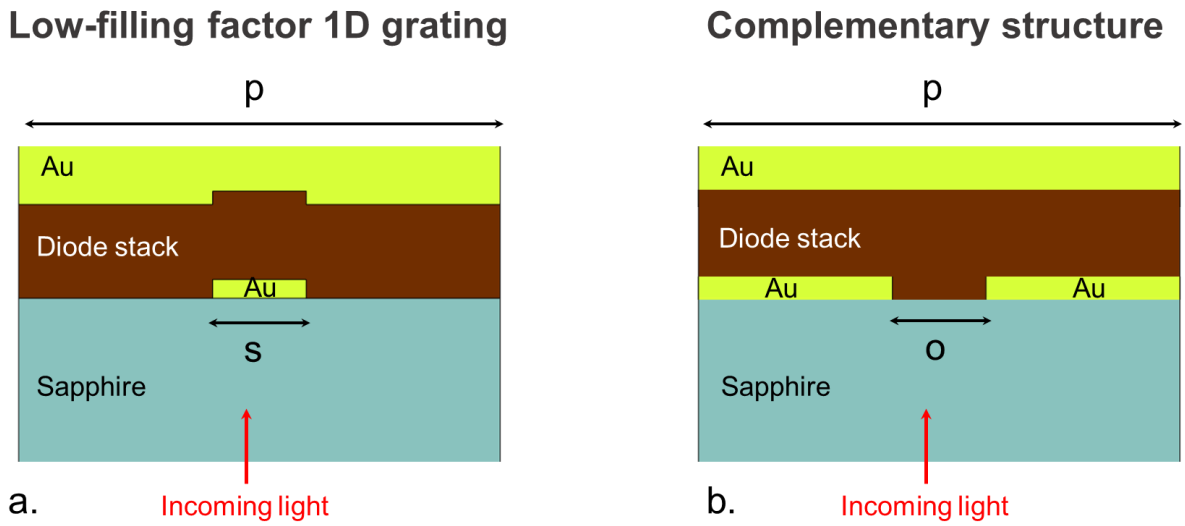

Figure S 2: Design of the high-filling factor grating. *a. A diode with the conventional low metal filling factor grating as the bottom electrode. b. A diode with the complementary grating structure with high metal filling factor as the bottom electrode.*

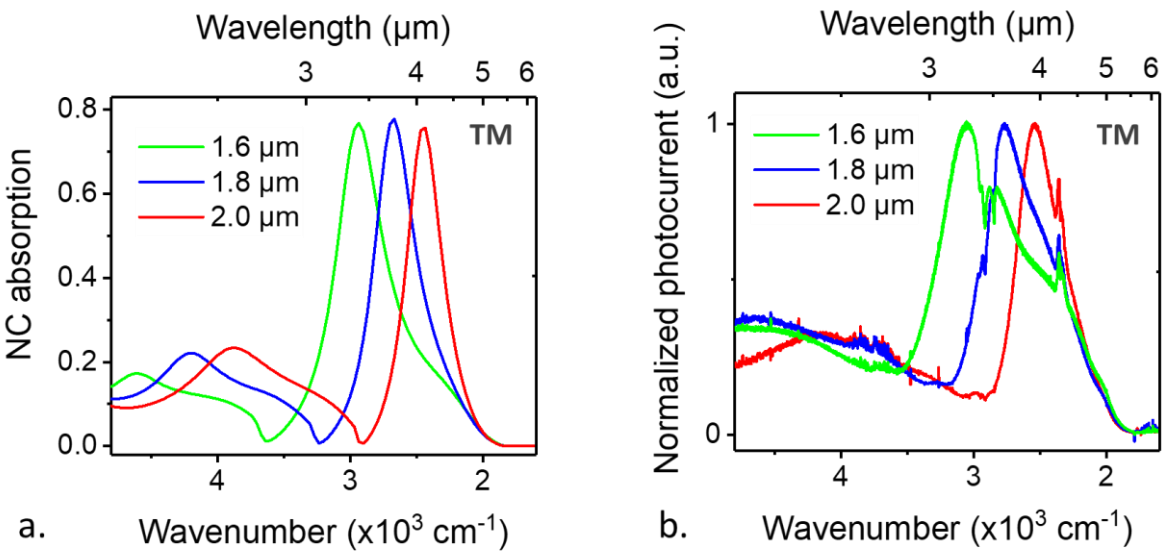

Figure S 3: Surface plasmon at normal incidence in diodes based on complementary bottom electrodes. *a. Simulated NC absorption in diodes with complementary bottom electrode with various periods. b. Measured photocurrent spectra of the diodes following the design of complementary bottom electrodes with various periods.*

Figure S 4 compares the absorption map and electric field distribution for low and high filling factor 1D gratings. There are two key differences. Firstly, a significant part of the absorption occurs away from the bottom metal electrode for the low-filling factor grating, as presented in **Figure S 4**a, while, for the high-filling factor one, absorption occurs between the top and bottom electrodes (**Figure S 4**b), making the latter more favorable for charge collection by avoiding additional planar transport (*i.e.*, lengthening of carrier diffusion pathways). Secondly, higher metal coverage for the bottom electrode reduces the leakage of the electromagnetic field into the substrate (resulting in reduced optical loss), as shown in **Figure S 4**d, in contrast to the conventional low-filling factor grating in **Figure S 4**c.

An important point when designing metal-based electrodes is to limit the optical loss in the metallic layers, which do not contribute to the photocurrent. Here, as our goal is to increase the metal filling factor of the electrode, we also need to ensure that the absorption in the metal layers does not increase. **Erreur ! Source du renvoi introuvable.** compares metal absorption in the low and high-filling factor gratings (*i.e.*, complementary structure). Over the spectral range of interest, the high-filling factor grating presents an average metal loss below 20 %.

It is interesting to note that, due to the high coverage of the bottom gold electrode in the complementary structure, the surface plasmon gets guided between two metallic layers, as shown in Figure S4d. In the following, we show that this mode is not the standard cavity mode observed in TM polarization in Metal-Insulator-Metal (MIM) cavities,[4,5] but it is similar to the surface plasmon mode shown in Figure S4c.

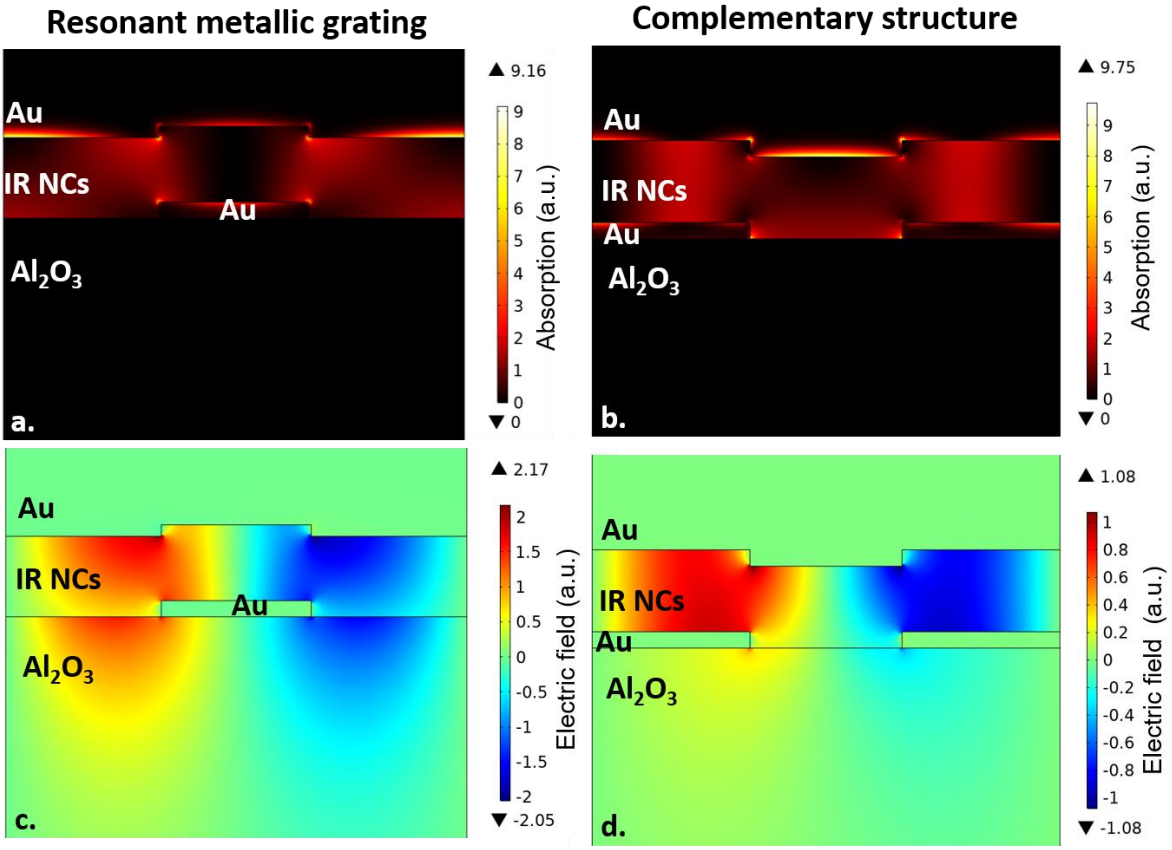

Figure S 4: **Field localization for the low and high-filling factor 1D gratings.** a. (resp c.) Absorption (resp. electric field) map for the low-filling factor grating structure. b. (resp. d.) Absorption (resp. electric field) map for the high-filling factor grating structure.

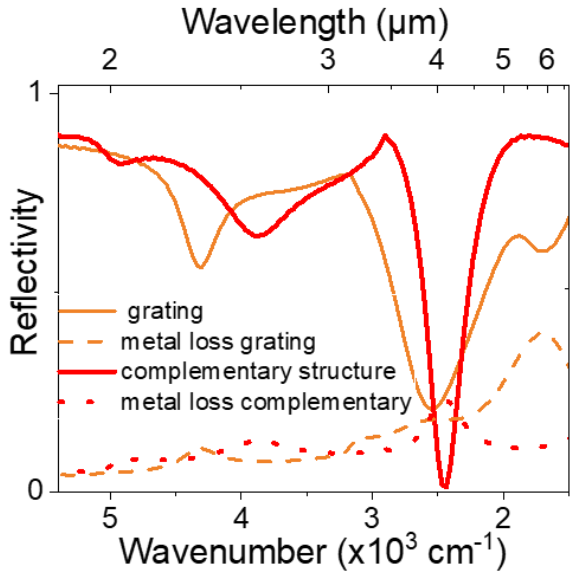

Figure S 5 : Optical losses in the metallic layers for low and high-filling factor 1D gratings. *Solid lines are the simulated reflectivity spectra for low-filling factor grating structure (orange) and complementary structure (red lines). Dashed lines are the*

optical losses occuring in metal for the low-filling factor grating structure (orange dashed lines) and the complementary structure (red dashed lines).

Resonant modes in MIM cavities are strongly localized and dispersionless (angle-independent), as their wavelength is set by the metallic stripes width s, $\lambda_{cavity} = 2 \cdot n_{eff} \cdot s$, with n_{eff} the effective index of the mode. Our previous studies showed that for the cavity mode to overlap with the NC band edge around 4 µm, the dimension s needs to be around 400-600 nm, depending on the NC film thickness.[4] In contrast, complementary structures have grating widths of around 1400-1600 nm. Thus, it is unlikely that the cavity mode is generated at 4 µm in our complementary structure. Indeed, in a complementary structure with a period of 2000 nm, changing the stripe width s from 1200 to 1600 nm does not significantly change the nanocrystal absorption spectrum, see **Figure S 6**.

The influence of the stripe width s is also highlighted in **Figure S 7**. Panel (a) presents the calculated dispersion of a grating with s=0.8µm and p=1.4µmn while panel (b) shows the dispersion obtained for s=1.35µm and p=1.6µm. In both cases, there is no signature of a cavity mode.

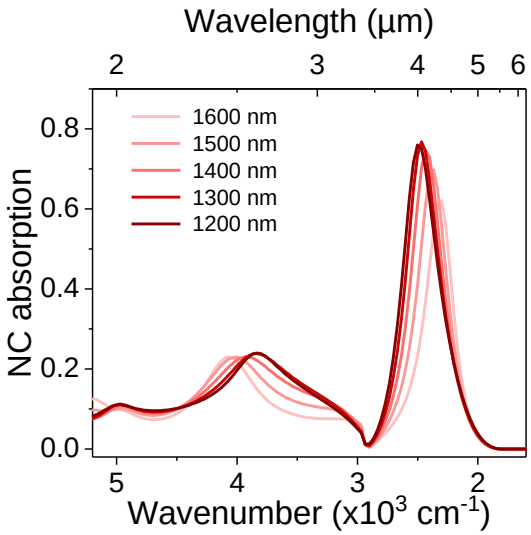

Figure S 6: Absorption spectra of nanocrystal films in complementary structures with different grating widths. *Grating period is kept constant at 2 µm, NC thickness is 350 nm.*

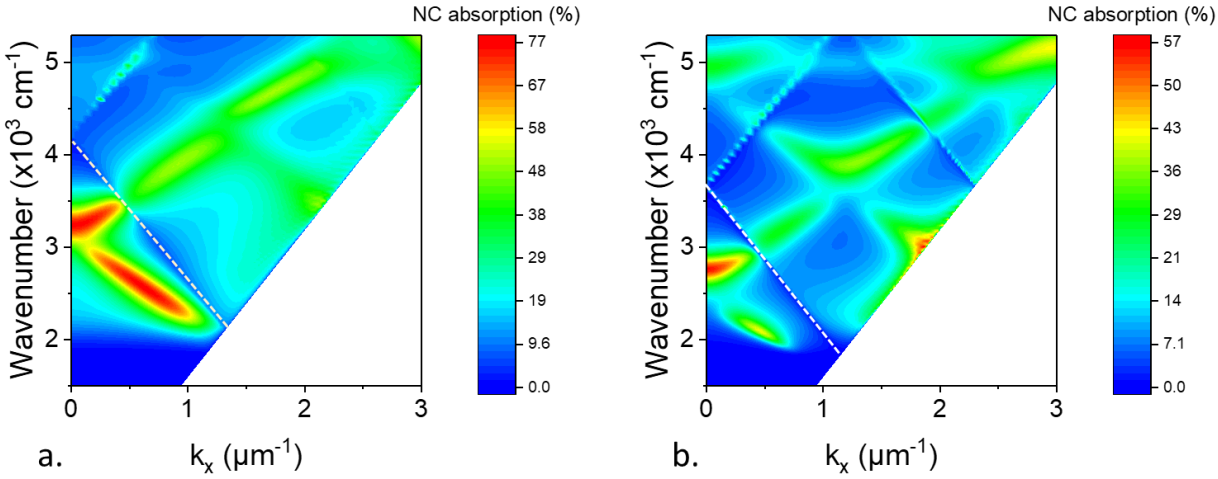

Figure S 7: Dispersion maps of structures with different grating periods. *a.* Dispersion map of a structure with a grating period p=1.4 µm and grating width s=0.8 µm. b. Dispersion map of a structure with a grating period p=1.6 µm and grating s=1.35 µm. The white dashed lines highlight the diffraction limits, which depend on the period of the grating. Above the diffraction limit, high-order diffraction leads to weakened overall NC absorption.

4. Design of the 2D metasurface

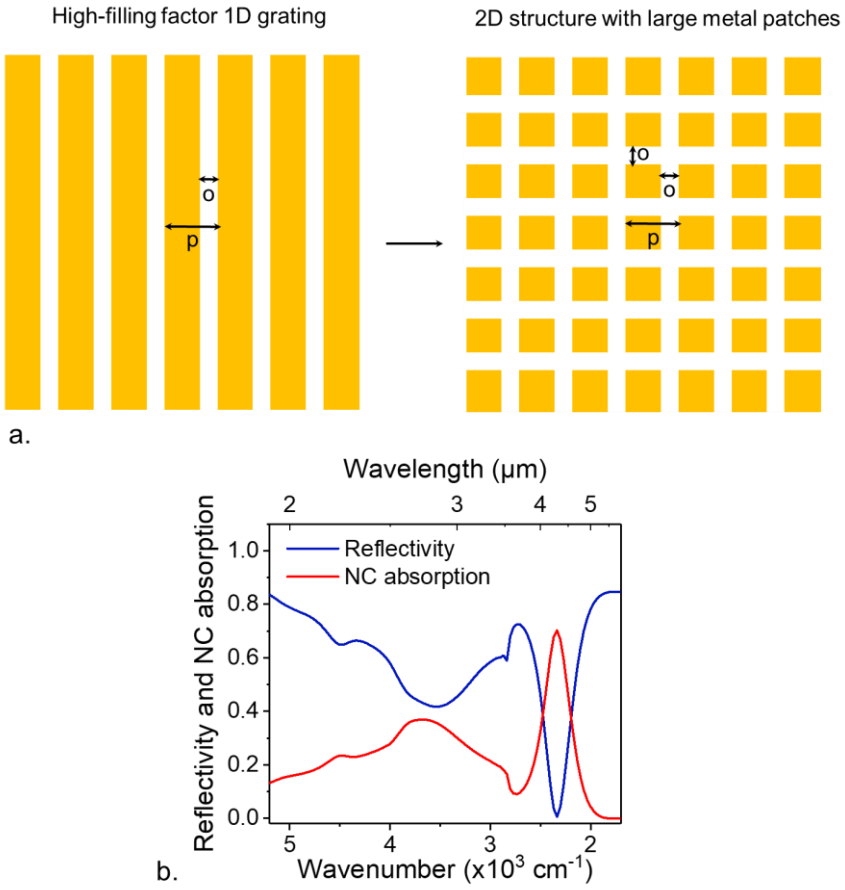

Figure S 8: Transformation of the 1D grating to 2D surface of large square patches. *a. 2D symmetrical surface is formed by adding perpendicular opening lines to the 1D grating. b. Simulated reflectivity and NC absorption of a diode with the 2D bottom electrode presented in panel (a.). Here, p = 2.2 μm, o = 0.6 μm.*

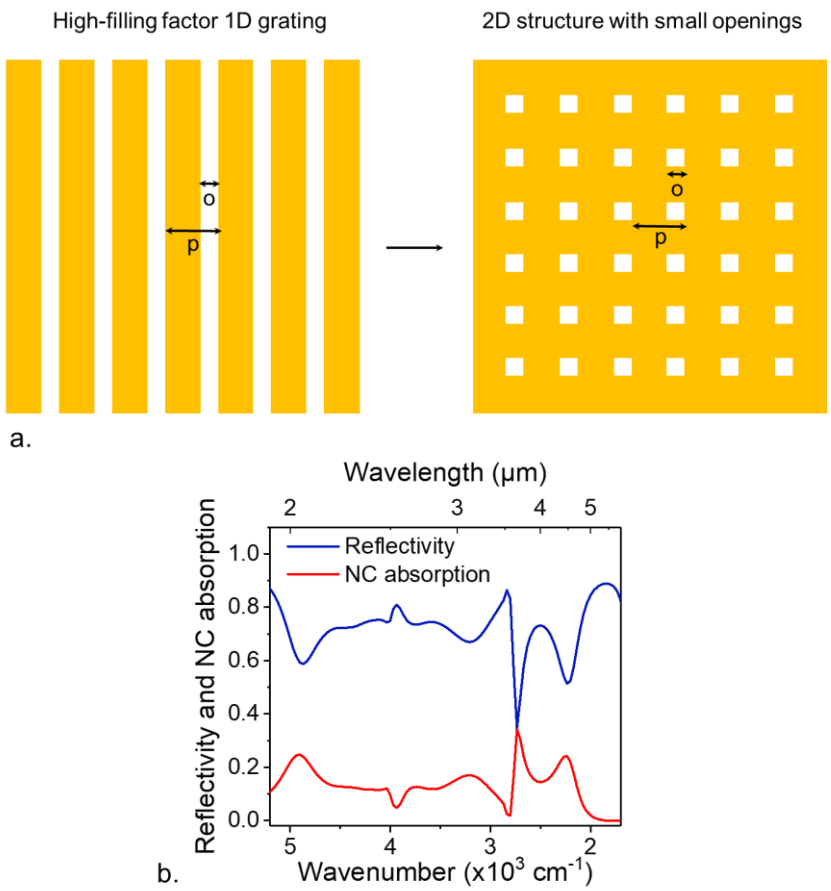

Figure S 9 **Transformation of the 1D grating to 2D surface with small square openings.** *a. 2D symmetrical surface is formed by adding perpendicular grating stripes to the 1D grating. b. Simulated reflectivity and NC absorption of a diode with the 2D bottom electrode shown in panel (a.). Here, p = 2.2 μm, o = 0.8 μm.*

A direct transformation strategy cannot be applied to ensure both high metal coverage and optical transmission. A surface consisting of large metal patches, illustrated in **Figure S 8**a, allows for maintaining a high metal coverage and good transmission. Particularly, a surface plasmon can be generated and gives rise to approximately 70% NC absorption, see **Figure S 8**b. However, this strategy leads to the discontinuity of the electrode, disallowing electrical connection. On the other hand, transforming the 1D grating to a 2D surface with small square openings (**Figure S 9**) limits the optical transmission of the electrode due to excessive metal coverage. As shown in **Figure S 9**b, such an electrode with p= 2.2 μm and o = 0.8 μm leads to a reflectivity of more than 60% of the diode stack.

To this end, we adopt the first step as the transformation in **Figure S 8**, then add interconnected wires between the large patches for electrical connection. The final structure is presented in **Figure 3**a. The structure generates a surface plasmon with the electric field enhancement in the area covered by the metal (**Figure 3**e), thus enabling a good overlap between the electromagnetic field and the diode's built-in electrostatic field. Using this strategy, we obtain a 2D metasurface with high metal coverage and good optical transmission.

5. Diode fabrication procedure

Figure S *10*a-f depict the main fabrication steps of the diode, while part g shows a scanning electron microscopy of the 2D metasurface.

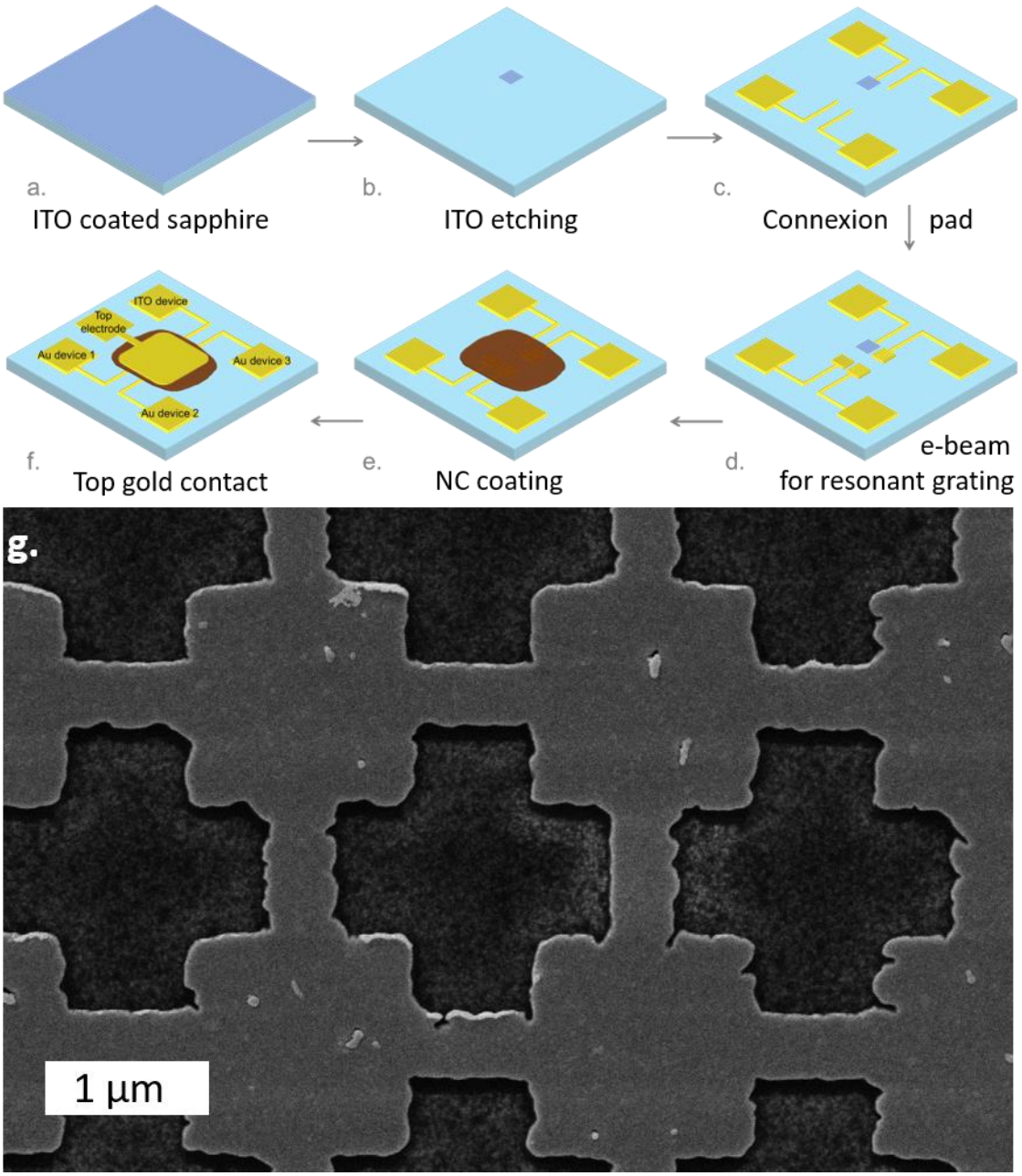

Figure S 10: ***Fabrication steps for the photodiode with 2D metasurface as partly transparent electrodes.*** *Steps a to f describes the fabrication steps for the diode. g. Scanning electron microscopy image of the 2D electrodes.*

6. Diode performances

Figure S 11 and **Figure S 12** provide characterization of the diode based on 2D metasurface bottom electrode.

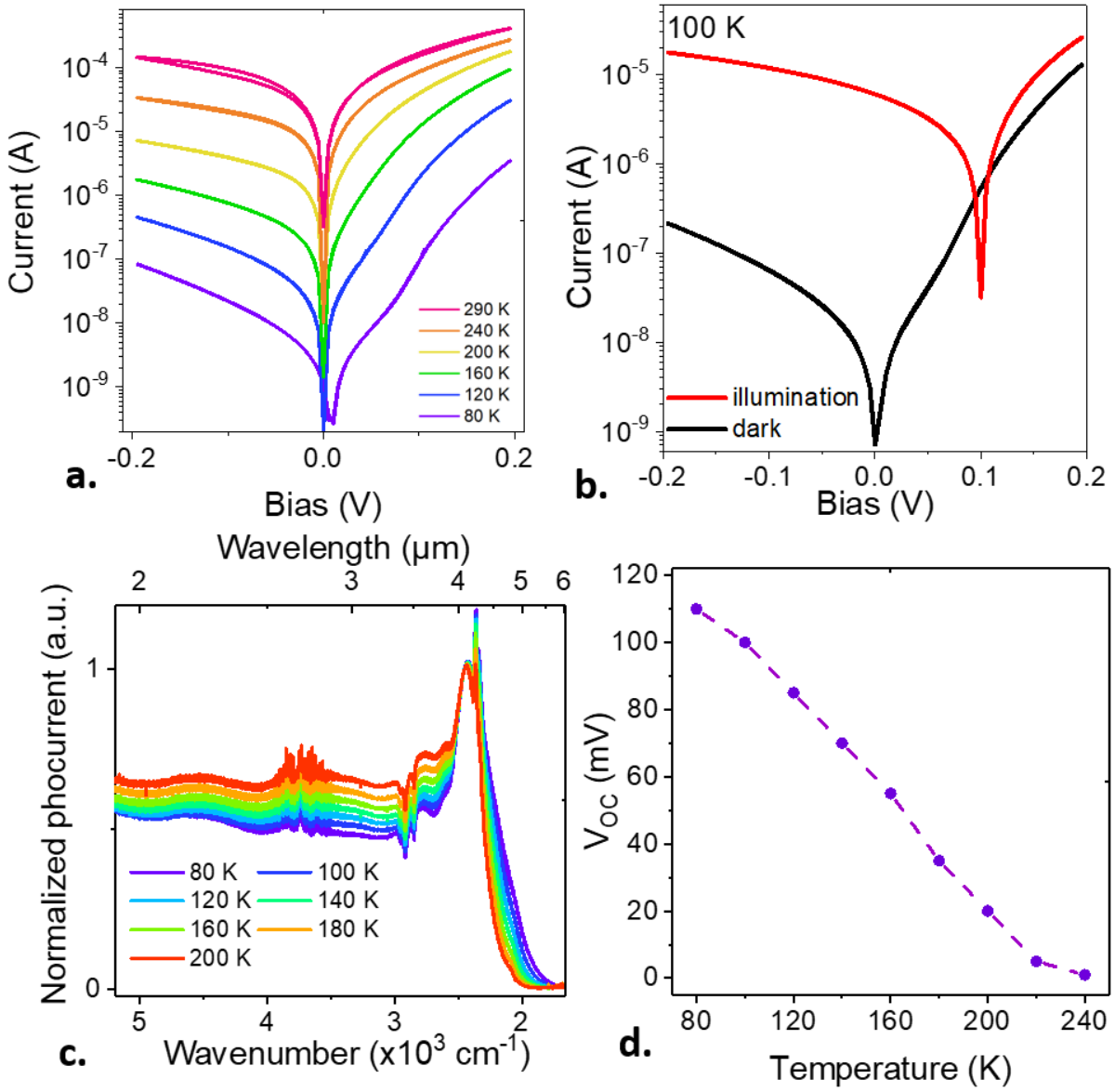

***Figure S 11: Characterization as mid IR sensor based on 2D crosses**. a. Dark IV curves at various temperatures. b. Dark and under illumination (using a quantum cascade laser opeating at 4.4 µm) IV curve acquired at 100 K. c. Photocurrent spectra at various temperatures. d. Open circuit voltage under illumination of a 4.4 µm quantum cascade laser, with nominal power of 15.6 mW at various temperatures..*

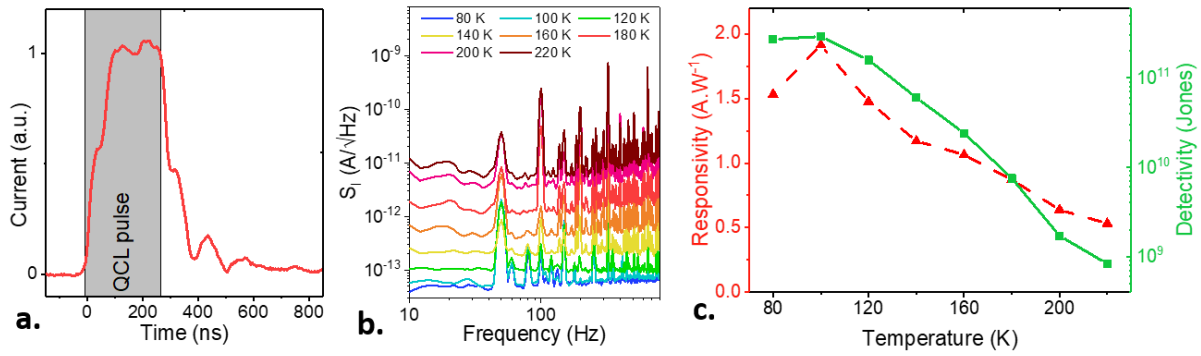

Figure S 12: Temporal and signal to noise determination for the mid IR sensor based on 2D crosses. *a. Current as a function of time under excitation of a 200 ns pulse by a 4.4 µm quantum cascade laser. b. Noise current spectral density at various temperatures. c. Responsivity and specific detectivity as a function of temperature. Light source is a black body at 600°C and measurements are conducted under 0 V applied bias voltage.*

7. References

(1) Ackerman, M. M.; Tang, X.; Guyot-Sionnest, P. Fast and Sensitive Colloidal Quantum Dot Mid-Wave Infrared Photodetectors. *ACS Nano* **2018**, *12* (7), 7264–7271. https://doi.org/10.1021/acsnano.8b03425.

(2) Moghaddam, N.; Gréboval, C.; Qu, J.; Chu, A.; Rastogi, P.; Livache, C.; Khalili, A.; Xu, X. Z.; Baptiste, B.; Klotz, S.; Fishman, G.; Capitani, F.; Ithurria, S.; Sauvage, S.; Lhuillier, E. The Strong Confinement Regime in HgTe Two-Dimensional Nanoplatelets. *J. Phys. Chem. C* **2020**, *124* (42), 23460–23468. https://doi.org/10.1021/acs.jpcc.0c07533.

(3) Lhuillier, E.; Keuleyan, S.; Guyot-Sionnest, P. Optical Properties of HgTe Colloidal Quantum Dots. *Nanotechnology* **2012**, *23* (17), 175705. https://doi.org/10.1088/0957-4484/23/17/175705.

(4) Dang, T. H.; Cavallo, M.; Khalili, A.; Dabard, C.; Bossavit, E.; Zhang, H.; Ledos, N.; Prado, Y.; Lafosse, X.; Abadie, C.; Gacemi, D.; Ithurria, S.; Vincent, G.; Todorov, Y.; Sirtori, C.; Vasanelli, A.; Lhuillier, E. Multiresonant Grating to Replace Transparent Conductive Oxide Electrode for Bias Selected Filtering of Infrared Photoresponse. *Nano Lett.* **2023**, *23* (18), 8539–8546. https://doi.org/10.1021/acs.nanolett.3c02306.

(5) Todorov, Y.; Tosetto, L.; Teissier, J.; Andrews, A. M.; Klang, P.; Colombelli, R.; Sagnes, I.; Strasser, G.; Sirtori, C. Optical Properties of Metal-Dielectric-Metal Microcavities in the THz Frequency Range. *Opt. Express* **2010**, *18* (13), 13886–13907. https://doi.org/10.1364/OE.18.013886.